University of Massachusetts Amherst

ScholarWorks@UMass Amherst

2009

DYNAMIC S0 GALAXIES: A CASE STUDY OF NGC 5866

J-T Li

QD Wang
University of Massachusetts - Amherst

Z Li

Y Chen

Follow this and additional works at: https://scholarworks.umass.edu/astro_faculty_pubs

Part of the Astrophysics and Astronomy Commons

Dynamic S0 Galaxies: a Case Study of NGC 5866

Jiang-Tao Li[1,2], Q. Daniel Wang[2], Zhiyuan Li[2,3], and Yang Chen[1]

ABSTRACT

S0 galaxies are often thought to be passively evolved from spirals after star formation is quenched. To explore what is actually occurring in such galaxies, we present a multi-wavelength case study of NGC 5866 — a nearby edge-on S0 galaxy in a relatively isolated environment. This study shows strong evidence for dynamic activities in the interstellar medium, which are most likely driven by supernova explosions in the galactic disk and bulge. Understanding these activities can have strong implications for studying the evolution of such galaxies. We utilize *Chandra*, *HST*, and *Spitzer* data as well as ground-based observations to characterize the content, structure, and physical state of the medium and its interplay with the stellar component in NGC 5866. A cold gas disk is detected with an exponential scale height of $\sim 10^2$ pc. Numerous distinct off-disk dusty spurs are also clearly present: prominent ones can extend as far as $\sim 3 \times 10^2$ pc from the galactic plane and are probably produced by *individual* SNe, whereas faint filaments can have $\sim$ kpc scale and are likely produced by SNe collectively in the disk/bulge. We also detect substantial amounts of diffuse Hα- and Pα-emitting gas with a comparable scale height as the cold gas. We find that the heating of the dust and warm ionized gas cannot be explained by the radiation from evolved stars alone, strongly indicating the presence of young stars in the galactic disk, though at a slow formation rate of ~ 0.05 M$_\odot$ yr^{-1}. We further reveal the presence of diffuse X-ray-emitting hot gas, which extends as far as 3.5 kpc away from the galactic plane and can be heated easily by Type Ia SNe in the bulge. However, the mean temperature of this gas is ~ 0.2 keV, substantially lower than what might be expected from the mass-loss of evolved stars and Type Ia SNe heating alone in the galaxy, indicating that the mass loading from the cool gas is important. The total masses of the cold, warm ionized, and hot gases are $\sim 5 \times 10^8$ M$_\odot$, 4×10^4 M$_\odot$ and 3×10^7 M$_\odot$, respectively. The relative richness of the gases, apparently undergoing circulations between the disk and halo of the galaxy, is perhaps a result of its relative isolation.

Subject headings: galaxies: general-galaxies: individual (NGC 5866)-galaxies: S0

---

[1]Department of Astronomy, Nanjing University, 22 Hankou Road, Nanjing 210093, P. R. China

[2]Department of Astronomy, University of Massachusetts, 710 North Pleasant Street, Amherst, MA 01003, U.S.A.

[3]Harvard-Smithsonian Center for Astrophysics, 60 Garden Street, Cambridge, MA 02138

1. Introduction

Living at the intersection of spirals and ellipticals on the Hubble tuning fork, lenticular (or S0) galaxies are often thought to be remnants of spirals after star formation (SF) has ceased (or has slowed down substantially). This transition in the SF rate (SFR) must be directly related to the change of cold gas content and/or density in the disk of such a galaxy. The change may be caused by such processes as (e.g., Martig et al. 2009 and references therein): ram-pressure stripping (of cold gas), termination or strangulation (removing surrounding hot gas, hence a source of new cold gas), morphological quenching (heating of a stellar disk or even transforming to a spheroid), and exhaustion (consuming gas via SF). While the ram-pressure stripping of the cold or hot gas is expected to work primarily in a dense environment (in galaxy clusters and possibly in rich groups), the morphological quenching via galaxy-galaxy mergers should be most effective in groups. The exhaustion, an internal process, can occur in both rich and poor environments. For example, this process may occur for a relatively isolated galaxy when its halo mass M_h grows to be $\gtrsim 10^{11}$ M$_\odot$ and its gas accretion mode turns from cold to hot (e.g., Kereš et al. 2005; Kereš & Hernquist 2009 and references therein). In general, more than one of these processes may be involved in the transition of a galaxy. Their relative importance cannot be determined easily; great uncertainty remains in our understanding of the processes, especially in terms of their interplay with various other galactic activities such as the feedback from stars and AGNs. While observational studies of galaxy transformation have been concentrated on stellar properties, theoretical efforts (or computational simulations) are primarily on gaseous components on galaxy scales. This gap must be bridged to make significant progress in the field.

Here we present a case study of the nearby edge-on S0 galaxy NGC 5866 (also referred as M 102 or "Spindle" galaxy; see Table 1 for the salient parameters). Our goal is to understand the potential role of the stellar energy and mass feedback in regulating the evolution of various gaseous components in this relatively isolated galaxy. NGC 5866 belongs to the poor group LGG 396 with a velocity dispersion of ~ 74 km s^{-1} (e.g., Mulchaey et al. 2003). Two gas-rich companions, NGC 5907 (Sc) and NGC 5879 (Sbc), are known to be located several hundred kpc away; their interactions with NGC 5866 should be minimal. So we can focus on internal activities of the galaxy. As will be discussed later, this isolated environment in the "field" may explain the relatively richness of molecular gas in the galaxy (Table 1; Welch & Sage 2003; Sage & Welch 2006) and its slow evolution with ongoing low-level SF many gigayears after a major merger. There is also no evidence for strong nuclear activity in the galaxy (Terashima & Wilson 2003); the nucleus is classified in optical to be an intermediate object between a weak H II region and a LINER (Ho, Filippenko & Sargent 1997). Therefore, we can examine the effect of the stellar feedback with little confusion from other potential sources of mechanical energy inputs. Furthermore, the nearly complete edge-on inclination of the galaxy is optimal for the study of the galactic disk/halo interaction. Indeed, archival *HST* optical images (first studied by Cantiello, Blakeslee & Raimondo 2007 for globular clusters) show numerous off-disk cold gas spurs, in addition to a well-defined dust lane. To our knowledge, no characterization of such spurs has ever been made for any S0 galaxies,

let alone their nature and role in the galactic gaseous evolution. A previous X-ray study based on *ROSAT* observation revealed that NGC 5866 is an X-ray faint galaxy and that the X-ray emission is dominated by stellar sources (Pellegrini 1994). There was also a study based on a snap-shot (2 ks) observation made with *Chandra* to see if an AGN is present in the galaxy (Terashima & Wilson 2003); only an upper limit of $\sim 4 \times 10^{38}$ ergs s^{-1} was obtained, assuming the distance of the galaxy to be ~ 15.3 Mpc (Pellegrini 2005). Our study is based on a later 34 ks *Chandra* observation (previously studied by David et al. 2006 in a sample of early-type galaxies), which allows us to resolve out much of the discrete source contribution and to examine the potentially diffuse X-ray emission from the galaxy. In short, with various available tracers (optical absorption as well as Hα/Pα, infrared (IR) and soft X-ray emissions), we can now characterize the cold molecular/atomic, warm ionized, dusty and hot phases of the interstellar medium (ISM) and explore their relationships with the stellar feedback in the galaxy.

The organization of the paper is as follows. In §2, we briefly describe various data sets used for our examinations (mainly *Chandra*, *HST*, and *Spitzer*). Spatial and spectral analysis of these multi-wavelength data is presented in §3. We discuss our results and their implications for understanding the energetics and dynamics of the gas phases in §4. We summarize the results and conclusions in §5.

2. Observation and Data Reduction

The *Chandra* observation of NGC 5866 was taken on Nov. 14, 2002. We reprocess the archived data for our study. After the removal of background flares, a total effective exposure of 24.3 ks remains. A "stowed background", normalized by the count rate in the 10-12 keV range, is used to account for the non-X-ray event contribution. Our study is based on the data from the ACIS-S3 chip, although part of the S2 chip data is also used for our source detection, which is performed in the broad (B, $0.3 - 7$ keV), soft (S, $0.3 - 1.5$ keV) and hard (H, $1.5 - 7$ keV) bands (Fig. 1), following the procedure detailed in Wang (2004). To study the diffuse X-ray emission, we remove detected discrete sources from the data. Circular regions are excluded within twice the 90 per cent energy enclosed radius (EER) around each source of a count rate $(CR) \lesssim 0.01$ cts s^{-1}. For brighter sources, the source removal radius is further multiplied by a factor of $1 + log(CR/0.01)$. Generally about 96 per cent of the source counts are excluded in such a removal. For our spectral analysis of the diffuse X-ray emission, we further remove a local sky background. This background spectrum is first extracted from the source-removed data in a region surrounding the galaxy (Fig. 1). The spectrum, with the stowed background subtracted, is modeled with a thermal plasma model (MEKAL in XSPEC) and a power-law (with a photon index of 1.4, Lumb et al. 2002), representing both the Galactic and extragalactic background contributions. This local sky background model, normalized for the relative area coverage, is to be subtracted from on-source spectral data.

We use *HST* ACS (pixel size$\sim 0\rlap{.}''05$) and NICMOS (pixel size$\sim 0\rlap{.}''2$) observations in both broad and narrow bands. An Hα image is constructed from the ACS on-line narrow band (F658N) and
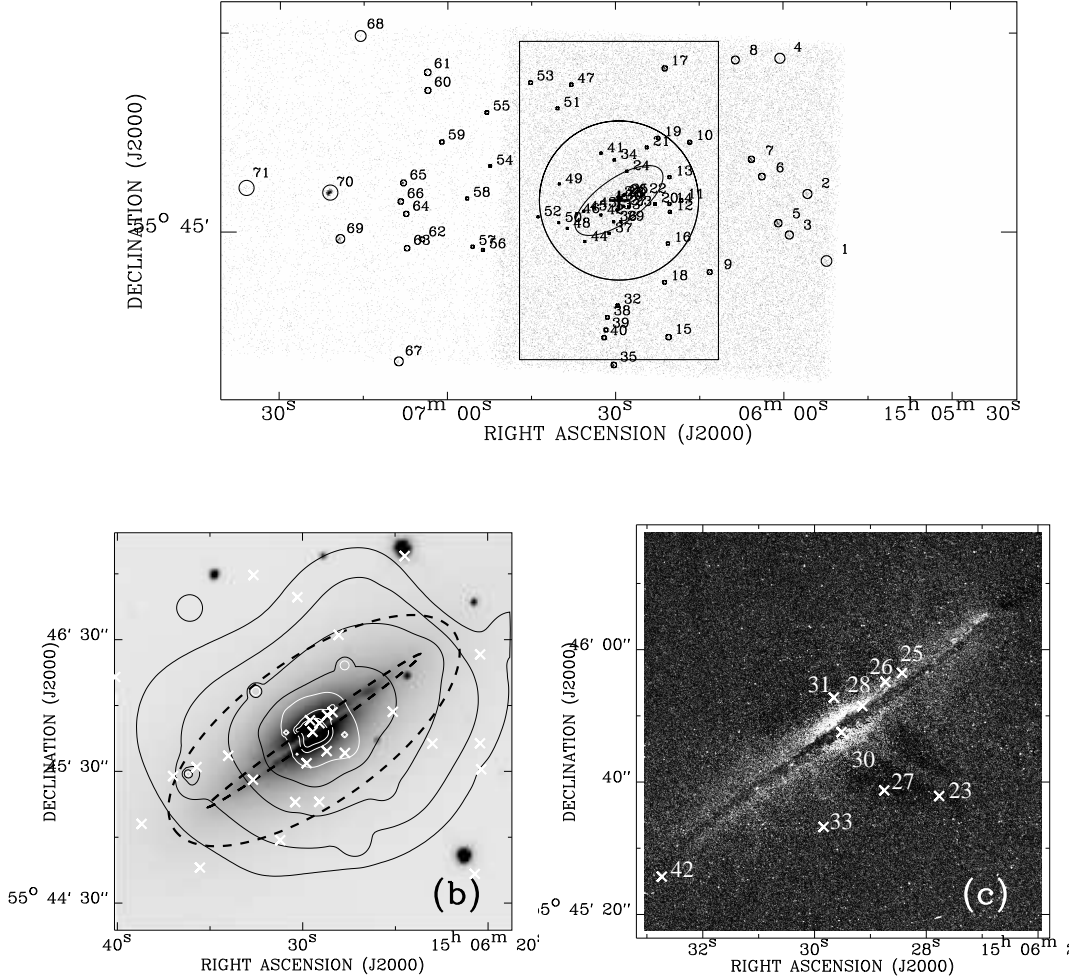
Fig. 1.— (a) *Chandra*/ACIS-S image of NGC 5866 in the 0.3-7 keV band. Detected sources are enclosed with circles of about 96% PSF (point spread function) EER and labeled with the numbers as in Table 2. The plus sign marks the center of the galaxy. While the ellipse marks the bulge region used for the spectral analysis, the field between the large circle and box is for the local sky background. (b) The central $3' \times 3'$ (9.7×9.7 kpc) of NGC 5866. Intensity contours of the source-removed emission in the ACIS-S 0.5-1.5 keV band overlaid on the SDSS R-band image of NGC 5866; the contours are at $(2, 3, 5, 10, 20, 55, 75) \times 10^{-3}$ cts s^{-1} arcmin^{-2}. The removed point sources are marked by crosses. The large dashed ellipse outlines the bulge region as in (a), while the small ellipse marks the region used to calculate the galactic disk mass. (c) Hα emission in the central region (the scale is the same as that in (b)) as described in §2 with X-ray sources marked as white crosses.

off-line broad band (F625W) observations. The off-line image, used for the continuum subtraction, is normalized by a factor of 0.09 to account for the bandwidth difference, which is determined by the average flux ratio of several bright foreground stars in the field (thought to have no Hα line emission). We further construct a Pα image from NICMOS data. The F190N continuum observation is directly subtracted from the on-line F187N observation because the two bands have approximately the same bandwidth; there is no bright foreground stars found in the small field of view in the NICMOS observations.

We further use archival *Spitzer* IRAC 3.6 μm, 8 μm and MIPS 24 μm images as well as 2MASS near-IR data. The 24 μm image is used to trace the dust emission, the stellar-light-subtracted 8 μm image is used to trace the PAH emission, while the 3.6 μm image and the 2MASS images are used to trace the emission from old stars. We make an aperture correction for the *Spitzer* images, following Dale et al. (2007). To subtract the old stellar contribution from the 8 μm emission, we adopt a ratio of 4.23 between the stellar light in 3.6 μm and 8 μm, since 3.6 μm emission in galaxies are dominated by old stellar light (Hunter et al. 2006). The pixel size of IRAC ($1''.2$) is smaller than that of MIPS 24 μm image ($2''.55$), so we rebin the 24 μm image to have the same pixel scale as the 3.6 μm image (but note that the resolution of MIPS at 24 μm is only $\sim 5''.9$), and plot them in Fig. 2c. The 2MASS near-IR image (with a spatial resolution of $\sim 1''$) is also dominated by old stellar light in galaxies, and the J-K color, as detailed in §4.1, is adopted as a tracer of the intrinsic extinction near the disk.

3. Analysis and Results

We present the *Chandra* ACIS-S intensity images of NGC 5866 in Fig. 1 (a and b). In particular, the morphology of the source-removed emission appears substantially rounder than that of the stellar bulge (Fig. 1b), clearly indicating the presence of non-stellar diffuse X-ray sources around the galaxy, probably hot gas. The emission is further compared to the optical and IR images in Fig. 2. The dusty disk is prominent in the optical images as absorption feature, with a diameter of $\sim 1'$ (3 kpc), less extended than the stellar disk which is also presented in the optical images (Fig. 2a). The dusty disk is slightly tilted from the stellar disk at the northwestern edge. In addition to the prominent dust lane, there are also lots of dusty spurs evidenced as extinction features in the optical images (Fig. 2a). Diffuse soft X-ray emission is found primarily in the bulge, while the Hα emission is strongest just off the dust lane (Fig. 2b). PAH and 24 μm emission is concentrated in the disk (Fig. 2c), in similar fashion as the extinction materials. But there is also a bright core on the 24 μm image (Fig. 2c), probably a nuclear SF region or a weak AGN.

Fig. 3 gives a more quantitative comparison of these various intensity distributions along the minor axis of the galaxy. It is clear that optical and soft X-ray intensities drop significantly toward the galactic plane within an off-plane distance of $|z| \sim 2''.4$ (130 pc, assume a distance of 11.21 Mpc as listed in Table 1 throughout the paper), due to the extinction and absorption by dusty gas in the galactic disk. We define distinct features outside this characteristic distance ($|z| \sim 2''.4 \sim 130$ pc) as

"extraplanar". Assume the diameter of the dusty disk to be $\sim 1'$ (3 kpc) and adopt the inclination angle in Table 1, the projected vertical extension of the dusty disk is $\sim 3''6$ (200 pc), so the region with $|z| \gtrsim 1''8$ (100 pc) is out of the dusty disk, comparable to our definition of the extraplanar region. In the following we detail the analysis and results from the data sets.
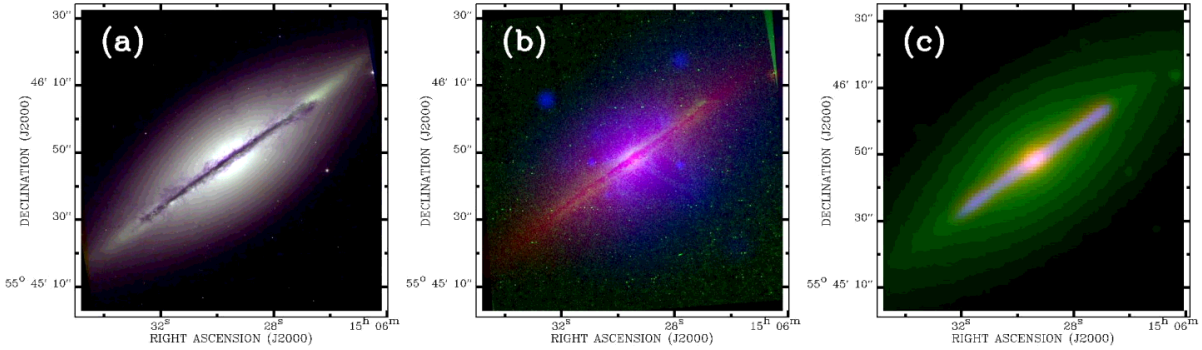

Fig. 2.— Tri-color images of the central $1'.5 \times 1'.5$ (4.9×4.9 kpc) of NGC 5866: (a) *HST* ACS F555W (*Red*), F435W (*Green*), and F658N (*Blue*); (b) *Spitzer* 3.6 μm (*Red*), *HST* Hα (*Green*), and *Chandra* source-removed intensity in the 0.5-1.5 keV band (*Blue*). (c) *Spitzer* 24 μm (*Red*), 3.6 μm (*Green*), and stellar-contribution-subtracted 8 μm (PAH, *Blue*).

3.1. Optical and Infrared Properties

We use the optical and infrared images to characterize the interstellar extinction as well as the cold and warm gas components in NGC 5866 (Figs. 1b, 2). Fig. 4 presents multi-wavelength images of the central region of the galaxy. An unsharp-masked (Howk & Savage 1997) B-band
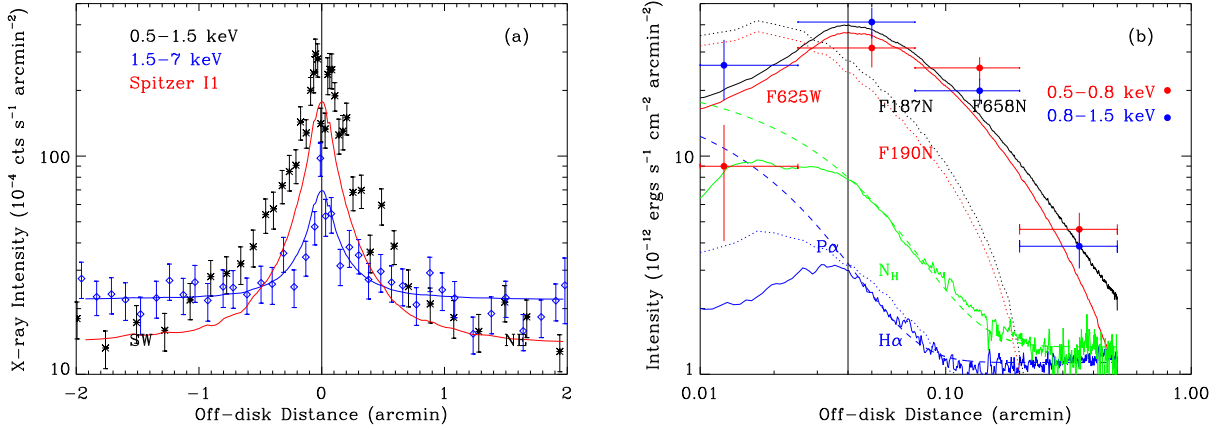
Fig. 3.— (a) Source-removed soft X-ray and near-IR intensity profiles along the minor axis. The full width along the major axis of the disk used for averaging the intensity is $3'$ (9.7 kpc). The *Spitzer* IRAC 3.6 μm intensity profile (blue solid line) is normalized to fit the 1.5-7 keV profile. The red solid line shows the old stellar contribution in 0.5-1.5 keV band, calculated using the *Spitzer* IRAC 3.6 μm intensity (see §3.2 for details). (b) The *Chandra* source-removed X-ray and *HST* optical intensity profiles calculated for the central region (see the text for details). The data on both sides of the major axis are averaged to increase the signal-to-noise ratio. The full width along the major axis of the disk used to average the intensities is $0\rlap{.}'5$ (1.6 kpc) for all the data in (b). The N_H profile calculated from the F435W and F555W data is plotted with an arbitrary normalization. This profile is only used to get the cold gas density scale height (see §3.1 for details). Both the Hα and N_H profiles are fitted with an exponential model (the dashed green and blue lines) in regions with $|z| \gtrsim 2\rlap{.}''4$ (130 pc, marked by the black vertical solid line, which marks the disk region where extinction is substantial).

image is constructed from the *HST* ACS F435W image. It is first smoothed with a median filter of a 51×51 pixel ($2\rlap{.}''5 \times 2\rlap{.}''5 \sim 135 \times 135$ pc) box and is then subtracted from the original image. This unsharp-masked image could emphasize structures on scales smaller than the smoothing box. As shown in Figs. 4a and 5, it highlights the filamentary structure of the extinction. In addition to the prominent central dust lane along the galactic disk, various prominent dusty spurs are located typically within $\sim 0\rlap{.}'1$ (3×10^2 pc) from the galactic plane. There is a shell-like dusty feature near the nucleus, with a diameter of $\sim 1\rlap{.}''8$ ($\sim 10^2$ pc) (Fig. 4a; i.e., Feature "04" in Fig. 5). The unsharp-masked image also shows more extended, but weaker extinction features in regions farther away from the mid-plane (up to $\sim$ kpc (1 kpc $\sim 0\rlap{.}'3$) scale; e.g., Feature "16" in Fig. 5).

For a distinct small-scale feature, we may estimate its extinction locally. The extinction at a
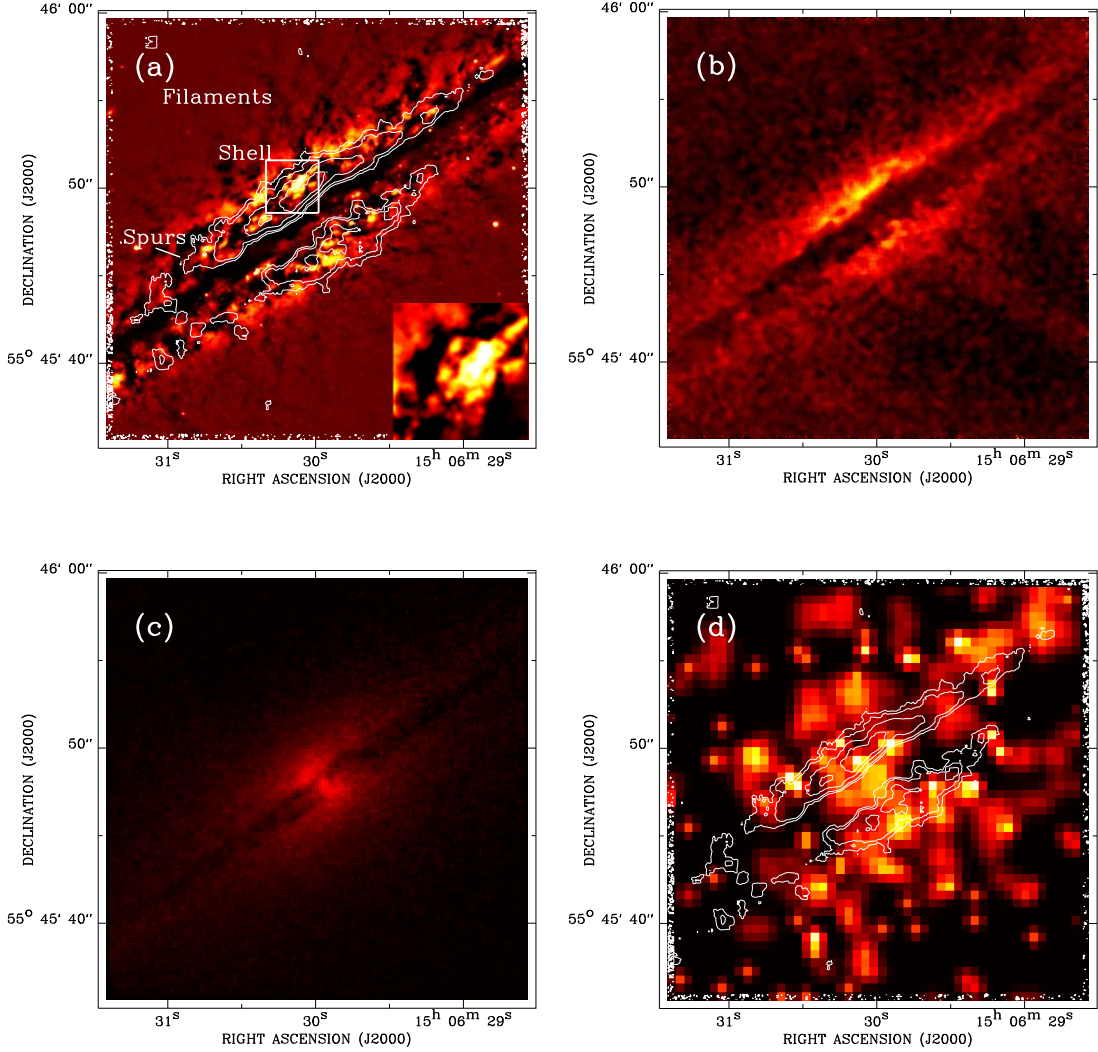
Fig. 4.— Multi-wavelength images of the central $0.\!'4 \times 0.\!'4$ (1.3×1.3 kpc) of NGC 5866. (a) Hα contours overlaid on the unsharp-masked F435W image. Various extinction features are marked. The white box encloses the central shell-like feature, which is viewed in a close-up at the lower right corner. (b) Smoothed Hα image as in (a). (c) Smoothed Pα image. (d) Hα contours as in (a) overlaid on the smoothed diffuse 0.5-1.5 keV image.

particular wavelength λ can be expressed as

$$a_\lambda = -2.5 \ log(S_{s,\lambda}/S_{b,\lambda}) \tag{1}$$

where $S_{s,\lambda}$ and $S_{b,\lambda}$ are the intensities on and off the feature (see also Howk & Savage 1997).

This estimation assumes that all the stellar light arises behind the feature, which is reasonable for the stellar bulge with a centrally concentrated light distribution. But in general, a_λ should be considered as a lower limit to the true extinction A_λ. We adopt the relation between the total neutral hydrogen column density and the color excess: $N_H = 5.8 \times 10^{21} \ E(B - V)$ atoms cm^{-2} (Bohlin, Savage & Drake 1978), assuming $R_V \equiv A_V/E(B - V) \approx 3.1$ and an extinction curve to convert A_λ to A_V (Cox 1999). We further assume that the depth of a dust feature is similar to its width and that the hydrogen to total mass conversion factor is 1.37, appropriate for gas of solar abundance. The resultant estimates of the hydrogen column density, number density and total mass are presented in Table 3. A typical spur has mass of $\sim 10^4 - 10^5$ M$_\odot$. We estimate that the mass of the extraplanar cold gas is $\sim 10^6 - 10^7$ M$_\odot$ in total, much smaller than the total cold gas mass estimated from CO observations ($\sim 5 \times 10^8$ M$_\odot$, Table 1). Thus most of the cold gas must have a smoother distribution, concentrated in the disk.
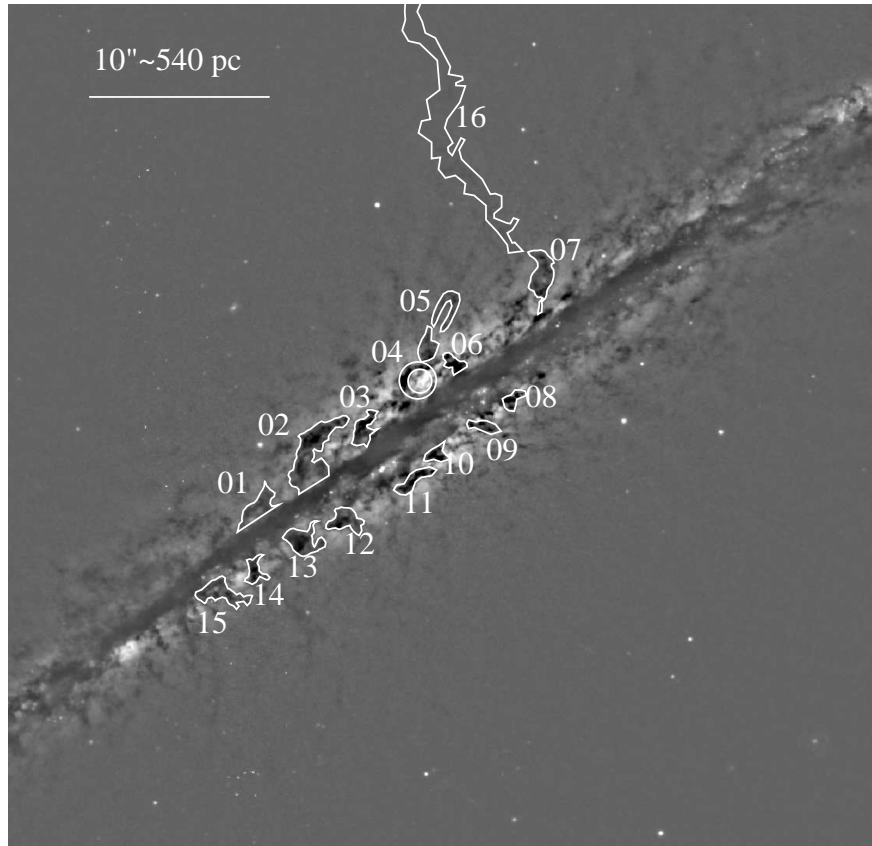

Fig. 5.— The unsharp-masked *HST* F435W image. Individual dust features are marked with numbers as listed in Table 3. The $10''$ bar shows the linear and angular scale of the image.

To characterize the global extinction as a function of the vertical distance z, we use the B-V

color calculated with the *HST* F435W and F555W images. The optical color cannot be an exact measure of the absorption column density when the intrinsic color is unknown or in an optical thick case. Here we just use the color to show the general distribution of the dusty gas and to give a crude estimate of the vertical scale height of the cold gas. As described above, $N_H \propto E(B - V)$, so it can be written as $N_H \approx a \times log\frac{S_V}{S_B} - b$, where S_V and S_B are the V- and B-band surface brightness, $a \approx 1.5 \times 10^{22}$ cm^{-2}, b is a parameter determined by the intrinsic color of the stellar population. Assuming a constant intrinsic color, the cold gas distribution is determined by the term $log\frac{S_V}{S_B}$, which is plotted in Fig. 3b and is fitted with an exponential model for the extraplanar region with $|z| \gtrsim 2''.4$ (130 pc). The scale height of the cold gas so obtained is $\sim 10^2$ pc. The flatten of the N_H profile in the central region with $|z| \lesssim 2''.4$ (130 pc) is due to the tilt of the disk, that is why we have defined regions with $|z| \gtrsim 2''.4$ (130 pc) as "extraplanar". The innermost trough of the N_H profile is caused by the extinction saturation in B-band.

Warm ionized gas, as traced by the Hα or Pα emission, shows a relatively smooth morphology and extends to $|z| \sim 300$ pc ($\sim 0'.1$) from the mid-plane (e.g., Fig. 3b, Fig. 4b,c). Although its overall distribution is similar to that of the dusty cold gas, there is little obvious feature-to-feature correlation. Indeed, some of the dusty features appear in regions with weak Hα emission (e.g., Feature "02" in Fig. 5). We fit the vertical distribution of the Hα emission, instead of Pα (because of the small field coverage of the NICMOS), in the region with $|z| \gtrsim 2''.4$ (130 pc) (Fig. 3b). The fitted exponential scale height is ~ 58 pc. Since the Hα intensity is proportional to n_{warm}^2, the scale height of the warm gas density should be $\sim 10^2$ pc, comparable to the scale height of the optical absorption features (or cold gas).

As the Hα emission suffers stronger extinction than the Pα emission, we use the Pα luminosity to estimate the recombination rate of the warm ionized gas. The total observed Pα luminosity in the region represented by the second X-ray data point at $|z| \sim 3''$ (160 pc) (Fig. 3b) is $(0.7 - 1.5) \times 10^{39}$ ergs s^{-1}, accounting for the uncertainty in the normalization factor of the continuum subtraction (§2) and corrected for the extinction. This luminosity corresponds to a recombination rate of $(4.3 - 9.6) \times 10^{51}$ s^{-1}.

3.2. X-ray Properties

We detect 15 point sources within the bulge region (Fig. 1). In particular, Source 30 coincides with the optical center of the galaxy (Fig. 1c). This source, detected only in the 1.5-7 keV band, has a count rate of 0.61 cts ks^{-1} (Table 2). Assuming a typical power law spectrum with a photon index of 1.7, we estimate the corresponding 1.5-7 keV luminosity as $\sim 1.2 \times 10^{38}$ ergs s^{-1}. The apparent strong soft X-ray absorption is consistent with the nucleus being behind the dusty disk. In any case, the low luminosity of the nucleus indicates that it is in a relatively quiescent state and probably has little impact mechanically on the global ISM of the galaxy. The spectrum of other sources outside the disk (Fig. 1b), the bulk of which should be LMXBs in the galactic bulge, can be represented by a power law of a photon index $\Gamma \approx 1.5$ and a very low absorption, consistent with the

Galactic foreground absorption value. Their integrated intrinsic luminosity is $\sim 3.8 \times 10^{38}$ ergs s^{-1} in the 0.5-2 keV band.

By removing the detected sources, we study the apparent diffuse emission. To isolate the truly diffuse hot gas in the galaxy, however, we need to quantify remaining stellar contributions: the emission from cataclysmic variables (CVs) and coronal active binaries (ABs) as well as the emission from unresolved LMXBs and the residual photons out of the discrete source removal circles (§2). We estimate the CV and AB contribution, 2.1×10^{38} ergs s^{-1}, from the calibrated ratio between the 0.5-2 keV luminosity and the bulge stellar mass ($\sim 7.0 \times 10^{27}$ ergs s^{-1} M$_\odot^{-1}$; Revnivtsev et al. 2008; refer to §4.1 for the estimation of the stellar mass). The contributions in other bands are calculated with a spectral model consisting of a 0.5 keV *MEKAL* optically-thin thermal plasma and a $\Gamma \approx 1.9$ power law (Revnivtsev et al. 2008). The residual emission from the source removal is $\sim 4\%$ of the detected source luminosity. The emission from unresolved LMXBs below our detection limit ($\sim 4 \times 10^{37}$ ergs s^{-1} in the 0.5-8 keV band) is estimated from the luminosity function of Gilfanov (2004), assuming the same spectrum as that for the detected sources. We then find that the total residual LMXB contribution is $\sim 3.3 \times 10^{38}$ ergs s^{-1} in 0.5-2 keV band. This contribution is confirmed independently from the spectral analysis of the diffuse emission, in which the normalization of the residual LMXB contribution is fitted (the luminosity of this component is fitted to be $\sim 2.9 \times 10^{38}$ ergs s^{-1} in 0.5-2 keV band, see below). These stellar contributions are added together and are assumed to have the same spatial distribution as the IRAC 3.6 μm intensity of the galaxy. They are then subtracted from the unresolved X-ray emission in spatial (Fig. 3a) and spectral (see below) analysis.

Fig. 3a compares the intensity distributions of the stellar contributions with the actually observed diffuse X-ray emission in the 0.5-1.5 keV and 1.5-7 keV bands. The two data points at the galactic plane in Fig. 3a shows large deviations from the global distribution of the 0.5-1.5 keV intensity profile. These deviations are clearly due to the absorption of soft X-ray by the cold gas disk. The stellar contribution as traced by near-IR emission matches well the observed 1.5-7 keV emission, indicating a stellar origin of the hard X-ray emission. Using the stellar contribution in 1.5-7 keV band as fitted and the spectral model of stellar sources adopted in the X-ray spectral analysis, we calculate the stellar contribution in 0.5-1.5 keV band (the red solid line in Fig. 3a). The excess of the observed 0.5-1.5 keV emission above the stellar contribution clearly shows the presence of the truly diffuse hot gas widespread in the galactic bulge, with a luminosity of $\sim 6.5 \times 10^{38}$ ergs s^{-1} in a region with $2\overset{''}{.}4$ (130 pc) $\lesssim |z| \lesssim 0\overset{'}{.}55$ (1.8 kpc) (roughly the bulge region shown in Fig. 1).

Fig. 6 presents the spectrum of the diffuse X-ray emission from the bulge, together with our best-fit model. In addition to the inclusion of the stellar contributions as described above, we model the hot gas emission as an optically-thin thermal plasma (*VMEKAL*). The fitted temperature of the plasma is $0.17^{+0.02}_{-0.03}$ keV. The Fe and O abundances are $3.5^{+1.4}_{-2.1}$ and $\lesssim 0.16$ solar. The inferred intrinsic luminosity of the hot gas $\sim 7.0 \times 10^{38}$ ergs s^{-1} in the 0.5-2 keV band is consistent with the above estimation based on the spatial distribution. The corresponding emission measure of the hot gas is ~ 0.07 cm^{-6} kpc^3. Note that the exact value of the metal abundance is somewhat

uncertain and is model-dependent due to the limited counting statistics and spectral resolution of the spectrum, but the assumption of isothermality typically leads to an under-estimate of the metal abundance. Therefore, the X-ray spectrum strongly indicates supersolar iron abundance, consistent with significant enrichment by Type Ia SNe.
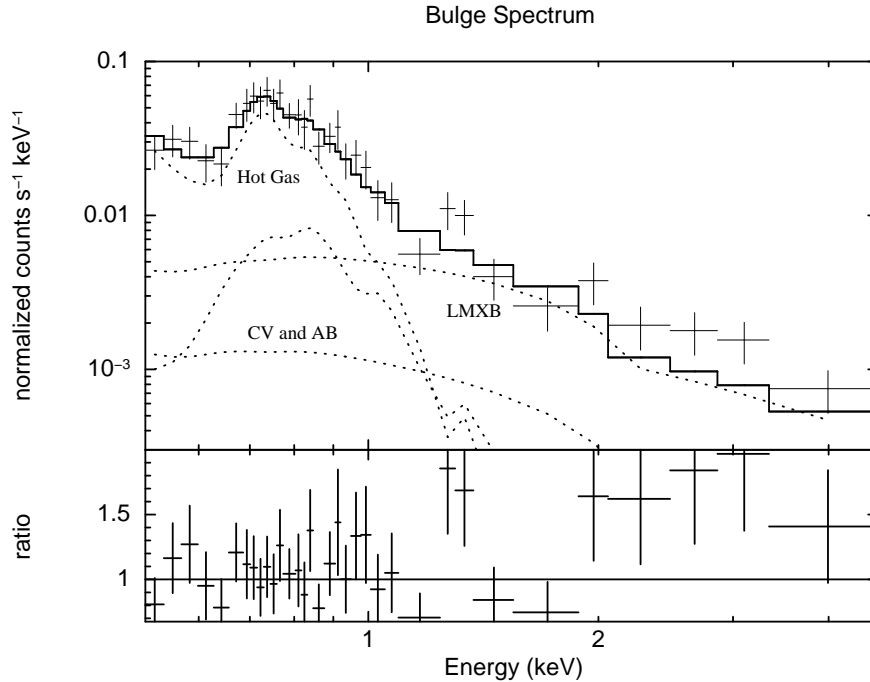
Fig. 6.— Spectrum of the diffuse X-ray emission from the bulge region. This spectrum is binned to achieve a signal-to-noise ratio better than 3 with respect to the best-fitted local background. It is also sky background and instrumental background subtracted. The best-fit model and its components (marked individually) are indicated by solid and dotted curves. Part of the residual photons from the model above 2 keV is due to some line features of the instrument particle signals (which is filtered during the fitting), although they are not clear on the figure, which is regrouped after subtracting the instrumental background. See text for details.

4. Discussion

Based on the above multi-wavelength characterizations of the stellar and interstellar components of NGC 5866, we now discuss their interplays, focusing on the physical state, dynamics, and evolution of the extraplanar gas. But first let us characterize the SF history of the galaxy, important for estimating the stellar mass and energy feedback.

4.1. Star formation history

For an S0 galaxy, we may assume that the bulk of stars is formed long ago during or before the last major merger that presumably forms the galactic bulge. One way to estimate the age of this merger is to use the globular cluster (GC) specific frequency (S_N), the number of GCs per unit luminosity in a given galaxy. GCs are believed to form in starbursts triggered by major mergers of gas-rich galaxies. Assuming that the evolution after mergers preserves the GC number, while the overall stellar luminosity of the galaxy may decrease with time. Therefore, S_N can be used as an age estimate for an S0 galaxy after its last merger and accompanied starburst (Barr et al. 2007). With $S_N \sim 1.4$ (Cantiello, Blakeslee & Raimondo 2007), we estimate the age of the NGC 5866 bulge to be ~ 8 Gyr, which is typical for S0 galaxies (Barr et al. 2007).

We now estimate the stellar mass of NGC 5866. Using the *2MASS* J- and K-band images, we get the J- and K-band intensity distributions. We further assume an optically thin case for near-IR emission, and an intrinsic color J-K=0.90, suitable for old stars in early type galaxies (Jarrett et al. 2003). We then map out the extinction value in different parts of the galaxy. Using the extinction-corrected K-band luminosity and adopting a color-dependent stellar mass-to-light ratio as detailed in Bell & de Jong (2001), we estimate the masses of the galactic bulge and disk regions (Fig. 1b) as $\sim 1.8 \times 10^{10}$ M$_\odot$ and $\sim 1.1 \times 10^{10}$ M$_\odot$.

There are lines of evidence for ongoing SF in the disk of NGC 5866. The most direct evidence comes from the observed 24 μm emission, which is usually thought to be mainly produced by hot dust heated by ultraviolet radiation, and is observed to concentrate in the cold gas disk in NGC 5866 (Fig. 2c). Such hot dust is found in both SF regions and circum-stellar material around evolved stars. The latter contribution, tightly correlated with the K-band luminosity in elliptical and S0 galaxies (e.g., Temi, Brighenti & Mathews 2007, 2009), is estimated to be $\sim 7 \times 10^{40}$ ergs s^{-1} for NGC 5866, significantly smaller than the total observed 24 μm luminosity of $\sim 3 \times 10^{41}$ ergs s^{-1} (excluding the nucleus which may be related to the AGN). This excess of 2.3×10^{41} ergs s^{-1} predicts an ongoing SF rate of ~ 0.05 M$_\odot$ yr^{-1} in the galactic disk. Here we have assumed that the relationship, SFR (M$_\odot$ yr^{-1}) $= 1.27 \times 10^{-38} [L_{24\ \mu m}(\ \text{ergs s}^{-1})]^{0.8850}$, obtained for active star forming galaxies (Calzetti et al. 2007), applies to NGC 5866. The low level of SF inferred here is consistent with the constraint (< 0.1 M$_\odot$ yr^{-1}) obtained from the model fit to the observed SED of NGC 5866 over the $\sim 2 - 10^3$ μm range (Draine et al. 2007). This means the SFR estimated using the mid-IR emission is reliable within the errors for NGC 5866, and further indicates that the MIPS 24 μm luminosity is mainly produced by the weak SF process in the disk.

The ongoing SF also explains the ionizing photon flux needed for producing the Pα luminosity. The relationship $L_{P\alpha} = 0.0049\ L_{24\ \mu m}$ (Rieke et al. 2009) gives a Pα luminosity of 1.1×10^{39} ergs s^{-1}, fully consistent with the observed value, $(0.7 - 1.5) \times 10^{39}$ ergs s^{-1}, which corresponds to a recombination rate of $(4.3 - 9.6) \times 10^{51}$ s^{-1} (§ 3.1). This may be a lower limit, since we may have still missed part of the Pα emission from the disk, due to its strong extinction. Alternatively, could the ionizing radiation be supplied by evolved stars? We use the ionizing radia-

tion with a rate of 7.3×10^{40} s^{-1} M$_\odot^{-1}$ for post-AGB stars (Binette et al. 1994) and 1.4×10^{40} s^{-1} M$_\odot^{-1}$ for hot horizontal branch stars (Han et al. 2007). Adopting the total stellar mass of the galaxy, $\sim 3 \times 10^{10}$ M$_\odot$ as inferred in §3.1, we estimate that the total expected hydrogen recombination rate for the galaxy is $\sim 3g_\star \times 10^{51}$ s^{-1}, where $g_\star$ is the fraction of the evolved ionizing photons intercepted by the gas. While most of the stars are in the galactic bulge, $g_\star$ should be considerably smaller than one. Therefore, the evolved stars alone seem to be insufficient to provide the ionizing photons. Furthermore, observed various emission lines such as [C II]$\lambda158\mu$m and [O I]$\lambda63\mu$m appear to be considerably stronger than what are expected from ionizing photons purely from the evolved stars (Malhotra et al. 2000, 2001).

Therefore, we conclude that the presence of low-level SF provides a unified explanation for the radiative heating and ionization of the dust and warm-ionized gas in NGC 5866.

4.2. Energetics of the extraplanar hot gas

Hot gas apparently dominates the extraplanar space. Adopting the spectral fit parameters in §3.2 and approximating the X-ray-emitting region as a cylindric volume with the radius $\sim 1\rlap{.}'3$ (4.2 kpc) and the hight $\sim 0\rlap{.}'55$ (1.8 kpc) (Fig. 1b), we estimate the mean density, thermal pressure, and radiative cooling time scale of the hot gas as ~ 0.065 cm^{-3}, $\sim 10^{-11}$ dyne cm^{-2}, and $\sim 1.5 \times 10^8$ yr. The total hot gas mass is $\sim 3 \times 10^7$ M$_\odot$. The estimation of these parameters are all based on the most reliable spectral fit parameters, i.e., the temperature, the luminosity and the emission measure of the thermal component (§3.2).

The most natural source of the gas that is subsequently heated is the mass loss of evolved stars. Assuming the mass loss by each planetary nebula (PN) is ~ 0.3 M$_\odot$ (Faber & Gallagher 1976), and using the PN birth rate in our Galaxy $\sim 11 \times 10^{-12}$ yr^{-1} L$_\odot^{-1}$ (Peimbert 1993), the mass loss rate (0.8 M$_\odot <$ M < 8 M$_\odot$) is 0.033×10^{-10} M$_\odot$ yr^{-1} L$_\odot^{-1}$. Adopting the stellar mass estimated in §4.1 and the age of ~ 8 Gyr (§4.1), the total mass return in NGC 5866 is then $\sim 8 \times 10^8$ $M_\odot$, which is substantially greater than what is observed in the hot gas. Furthermore, the mass-averaged Fe abundance as estimated from the mass loss of the evolved stars and metal enrichment of the Type Ia SN ejecta is about 6 times the solar value (Grevesse & Suval 1998), much larger than our spectral fit result (§3.2). One possibility of this relatively low observed Fe abundance is that the bulk of the Fe-rich SN ejecta is being blown out of the bulge before being fully mixed with the materials from the stellar mass loss (Tang et al. 2009).

To see if the heating provided by Type Ia SNe is sufficient to explain the X-ray cooling luminosity, we compare the X-ray luminosity with the SN heating rate. The supersolar iron abundance, as inferred from the spectral analysis of the hot gas, is consistent with heating primarily by Type Ia SNe. Assuming that each SN releases 10^{51} ergs and using the empirical Type Ia SN rate of Mannucci et al. (2005), which can be approximately expressed as 4.4×10^{-4} $(M/10^{10}$ M$_\odot)$ yr^{-1}, and the stellar mass $\sim 2.9 \times 10^{10}$ M$_\odot$ (§4.1), we estimate the total Type Ia SN rate of 1.3×10^{-3} SN yr^{-1}

and the mechanical energy injection rate as $\dot{E}_{SNIa} \sim 4 \times 10^{40}$ ergs s^{-1}. This energy injection rate is nearly two orders of magnitude greater than the X-ray luminosity! While a fraction of the energy injected into the cool gas disk may be radiated in other energy bands (e.g., extreme- and far-UV), avoiding a detection so far, the general lack of cool gas in the galactic bulge makes it hard to hide and convert the mechanical energy. Therefore, there is a missing stellar feedback problem in NGC 5866, similar to situations in other low-to-intermediate mass early-type galaxies (e.g. Li, Wang & Hameed 2007; Li, & Wang 2008; David et al. 2006). This missing stellar feedback indicates the presence of an outflow from the galactic bulge.

The dynamics of this outflow depends critically on the mass-loading from the cool gas disk, which is indicated by the observed low temperature of the hot gas in NGC 5866. The specific enthalpy of the stellar feedback, ~ 4 keV per particle, would give an average gas temperature of ~ 3 keV at the bulge center, which is substantially greater than ~ 0.17 keV inferred from the X-ray spectrum of the bulge (§3.2). In the inner bulge, the kinetic energy is often negligible compared to the thermal energy of the hot gas (Tang et al. 2009), so it cannot account for this large temperature difference. Part of the difference can be attributed to the SN energy stored in other forms (possibly magnetic field and cosmic rays as well as turbulent motion), the equal-partition among which may account for a factor up to 3-4. The emission measure-weighted temperature, as in the X-ray spectral analysis, also tends to under-estimate the real gas temperature by a factor ~ 2 (Tang et al. 2009). At least an additional factor of 2-3 is needed to explain our measured low temperature. This factor can be naturally explained by the mass-loading from the cool gas disk, as evidenced by the presence of extraplanar warm-ionized gas and dusty spurs, which represent the interface between the hot gas in the bulge and the cool gas in the disk.

4.3. Energetics of the extraplanar cool gas

Assuming a temperature of $\sim 10^4$ K and an approximate pressure balance with the hot gas, we estimate the parameters of the warm ionized gas based on the observed Pα emission measure. The volume filling factor, number density and total mass of the warm gas estimated this way are $\sim 10^{-4}$, 10 cm^{-3} and 10^4 M$_\odot$. The total mass is roughly consistent with the value of 4×10^4 M$_\odot$ as listed in Table 1. However, the number density is too high compared to that in other nearby galaxies (e.g. Collins et al. 2000), indicating that the warm and hot gas may be not in a pressure balance state, or the warm ionized gas may present as skins of some unresolved cool gas filaments.

Similar dusty spurs and their correlation with the extraplanar ionized gas have been observed previously in nearby edge-on *active star-forming* galaxies (e.g., Howk & Savage 1999; Li et al. 2008; Rossa et al. 2008). In particular, Howk & Savage (1997) have presented several mechanisms for the formation of extraplanar dusty features observed in NGC 891. These mechanisms include hydrodynamical processes like galactic fountain, radiation pressure driven outflow, and magnetic instability presumably induced by the differential rotation of galactic gaseous disks. The galactic fountain, the radiation pressure, and some magnetic instabilities like the Parker instability are

closely related to recent star forming activities. This is consistent with an apparent correlation between the amount of extraplanar gas and the SF rate of galaxies (Lehnert & Heckman 1996).

The heights and masses of the extraplanar cold gas features in NGC 5866 are significantly smaller than that in late-type galaxies (Howk & Savage 1999). Thus the processes responsible for producing the features are probably less energetic and would be overwhelmed in an active star forming galaxy. The very detection of the extraplanar extinction features in NGC 5866 is largely due to its nearly perfect edge-on perspective and its prominent stellar bulge background light. To check out the mechanical energy requirement for the extraplanar extinction features, we estimate their gravitational potential energies. Following Howk & Savage (1997), we estimate the energy Ω of a feature at height z from the mid-plane as:

$$\Omega = 10^{52} \ (\frac{M_c}{10^5 \ \mathrm{M_\odot}})(\frac{z_0}{300 \ \mathrm{pc}})^2(\frac{\rho_0}{1 \ \mathrm{M_\odot} \ \mathrm{pc}^{-3}})\ln[\cosh(z/z_0)] \ \mathrm{ergs} \tag{2}$$

where M_c is the mass of the cold gas feature, z_0 is the scale height of the mass density and is taken to be ~ 300 pc ($\sim 0\rlap{.}'1$), and $\rho_0 \sim 8.5$ M$_\odot$ pc^{-3} is the mass density at the mid-plane derived from the mass of the stellar disk (§4.1) and its size. The estimated gravitational potential energies for individual spurs are included in Table 3.

The mechanical energy needed to overcome the gravitational potential energy for an individual spur is mostly comparable to that expected for a single SN. Some of the spurs may represent super-impositions of multiple features. In such cases, the required energy could be considerably less. So in principle such spurs can be produced by individual SNe (e.g., Raley, Shelton & Plewa 2007), although some may be due to concerted energy inputs from massive stars, which may be formed in small groups or associations in NGC 5866. Using the empirical SFR-dependent relationship of Cappellaro, Evans & Turatto (1999), we estimate the core collapsed SN rate as 5×10^{-4} SN yr^{-1}, which is smaller than the Type Ia SN rate of 1.3×10^{-3} SN yr^{-1} as estimated in §4.2. Thus in NGC 5866, Type Ia SNe may be the primary energy source of the extraplanar dusty spurs, although core collapsed SNe can also be important. In contrast, the required energy for a high-z cold gas feature in late-type galaxies typically equals tens or hundreds of the SN energy (Howk & Savage 1997, 1999; Thompson, Howk & Savage 2004). This large energy requirement means most of the high-z cold gas features in these galaxies should be produced by the concerted energy injection from massive star forming regions. Similarly, large scale cold gas filaments (e.g., Feature "16" in Fig. 5) detected in NGC 5866 also require substantially more energy to form. They are probably produced by mechanical energy inputs provided collectively by core collapsed SNe in the disk and/or Type Ia SNe in the bulge of the galaxy.

4.4. Gas circulation between the galactic disk and halo

We further estimate the disk mass loss rate via outflows as indicated by the extraplanar dusty spurs in NGC 5866. From the simulation of extraplanar SNe driven disk outflow (Raley,

Shelton & Plewa 2007), the typical timescale to form an extraplanar cold gas spur through SNe driven hydrodynamical processes is $\sim 10^7$ yr. From the mass of the observed extraplanar cool gas ($\sim 5 \times 10^6$ M$_\odot$; §3.1), we infer the disk mass loss rate as ~ 0.5 M$_\odot$ yr^{-1}. A mass-loading to the hot phase at a comparable rate can naturally explain the low temperature of the hot gas (§4.2). But, assume a constant mass-loss rate of ~ 0.5 M$_\odot$ yr^{-1}, the disk would have lost $\sim 4 \times 10^9$ M$_\odot$ over 8 Gyr, which is an order of magnitude more than what remains in the disk. The current mass loss from the disk is driven by individual SNe (§4.3), a scenario different from that assumed for more energetic features detected in more active star forming galaxies. However, during the evolution of the galaxy, different processes (e.g. Type Ia SNe and SF) may dominate in different stages, so the mass loss rate may not be constant. In addition, accretion of cold gas from the intergalactic space could to some degree replenish the mass loss from the cold gas disk, which will also affect the observed amount of cold gas in the disk.

Some of the outflowing hot gas will eventually cool and return to the disk. Indeed, the mass-loaded hot gas with a temperature of ~ 0.17 keV is not expected to escape the gravitational potential of the galaxy. The corresponding sound speed of the hot gas is only about $c_s \simeq 150$ km s^{-1}, which is considerably smaller than the escape velocity, which should roughly be about three times of the circular velocity (~ 265 km s^{-1}; Neistein et al. 1999) for a typical dark halo potential. In this case, the hot gas will be confined by the gravitational potential of the galactic halo. The outflow is likely to be subsonic, explaining the moderate X-ray luminosity of the hot gas emission from NGC 5866 (Tang et al. 2009). The upper limit to the outflow speed, v, may be estimated from the accumulation time scale ($\gtrsim 5 \times 10^7$ yrs) of the hot gas in the bulge via the mass loss of evolved stars and from the cool gas mass loading from the disk. The lower limit can be set to have the cooling time scale ($\sim 1.5 \times 10^8$ yrs) of the hot gas longer than its escape time scale, assuming a characteristic bulge X-ray emission radius to be ~ 3 kpc. We thus have $0.4c_s \gtrsim v \gtrsim 0.1c_s$. The gas will cool in the large-scale galactic halo and will eventually return to the disk/bulge of the galaxy, which may be partly responsible for the present dusty galactic disk. Therefore, we expect a gas circulation, or a halo fountain (i.e., an outflow of heated gas to the halo and an inflow of cool gas to the disk/bulge), some of the extraplanar dusty structures may be such cool gas inflow (Fig. 5).

4.5.   Formation and evolution of field S0 galaxies

Now let us see how NGC 5866 may fit into the existing picture of galaxy formation and evolution. S0 galaxies in general are believed to be evolved from spirals when they have exhausted gas for massive SF. Much of the existing work has been focused on S0 galaxies in cluster environments, where the exhaustion of the gas is typically attributed to the ram-pressure stripping by the ambient medium (e.g. van Dokkum et al. 1998; Bekki, Couch & Shioya 2002; Goto et al. 2003; Moran et al. 2006). Outside clusters, the ram-pressure is unlikely to be strong enough to remove cool gas from galactic disks, although it may still be important in stripping gas from extended galactic halos and/or regulating the accretion from the intergalactic medium (IGM; e.g.,

Kawata & Mulchaey 2008). The evolution of such a field galaxy at present is typically dominated by internal processes, with galactic mass as the key parameter, according to recent simulations of galaxy formation (Birnboim & Dekel 2003; Birnboim et al. 2007; Kereš et al. 2005, 2009). A galaxy with $M_{halo} \gtrsim 10^{11}$ M$_\odot$ is expected to obtain its gas primarily in a so-called hot mode, in which accreted gas gets shock-heated near the virial radius to $T \gtrsim 10^6$ K. This virial shock presumably does not develop in lower mass galaxies, and the accretion is in a cold mode, in which the gas flows along narrow filaments that extend well inside the virial radius. This simple picture may provide a natural interpretation for the observed galaxy bi-modality of stellar color and morphology, although complications arise when galaxy-galaxy mergers and galactic feedback are considered. In this evolution picture, S0 galaxies may be a direct result of their mass growth, passing through the mass threshold, through mergers and/or accretion.

However, a field S0 galaxy formed this way (shutting off the cool gas supply) is expected to contain certain amount of cool gas in the galactic disk. In addition to the accumulation of the stellar mass loss, as discussed earlier, we also expect residual gas in the galactic disk from past SF. The consumption via SF becomes inefficient as the amount of cool gas slowly decreases (e.g., considering the Schmidt-Kennicutt Law and the Toomre column density criterion of SF; Kennicutt 1998; Toomre 1964). So substantial amounts of the disk gas should remain when the SF has more or less ceased, which may be the case for NGC 5866 and other field S0 galaxies (e.g., Sage & Welch 2006). Of course, as demonstrated in the present work, the feedback from old stars in the galactic disk and bulge, though relatively gentle, is long lasting, which can help to evaporate the cool gas disk. The effectiveness of this process on the long run depends on whether or not the evaporated gas can cool and then fall back into the disk, which is in turn sensitive to the intergalactic ram-pressure that the gaseous halo is subject to. NGC 5866 is relatively rich in cool gas as an S0 galaxy (Welch & Sage 2003; Sage & Welch 2006), which may be due to a lower than average ram-pressure — a result of the galaxy's relative isolation in a low-density environment. How the environment and S0 galaxy evolution affect the gas content and other galactic properties will be discussed in a following paper.

5. Summary

We have presented a multi-wavelength study of the edge-on S0 galaxy NGC 5866 in a very low density environment. We characterize various stellar and gaseous components and discuss the galactic disk/halo interaction and its role in the evolution of S0 galaxies. The main results are as follows:

- Based on a *Chandra* ACIS observation, we detect 15 point-like sources within the galactic bulge of the galaxy. One of them, with a 1.5-7 keV luminosity of $\sim 1.2 \times 10^{38}$ ergs s^{-1}, probably represents a very weak AGN of the galaxy.

- After removing the detected sources and subtracting remaining stellar contributions, we reveal

the X-ray emission from the diffuse hot gas in and around the galactic bulge. The emission extends as far as 3.5 kpc away from the galactic plane and has a total luminosity of $\sim 7 \times 10^{38}$ ergs s^{-1} in 0.5-2 keV. With a characteristic temperature of ~ 0.2 keV and a total mass of $\sim 3 \times 10^7$ M$_\odot$, the hot gas most likely represents a combination of the expected stellar mass loss and the mass-loading from the cool gas disk of the galaxy. The hot gas is over-abundant in iron and under-abundant in oxygen, indicating a strong chemical enrichment by Type Ia SNe.

- We detect warm ionized gas based on *HST* observations of Hα/Pα emission. This gas has an exponential scale height of $\sim 10^2$ pc and extends as far as $|z| \sim 3 \times 10^2$ pc from the mid-plane, indicating the presence of an extraplanar component. Massive stars in the galactic disk are primarily responsible for the ionization of this warm ionized gas.

- We characterize numerous cold gas features off the galactic disk, based on their extinction against the bulge stellar light. Dusty spurs typically have extensions similar to the warm ionized gas and have individual masses of $\sim 10^{4-5}$ M$_\odot$. Such spurs may be generated mostly by individual SNe in the galactic disk. But there are also more energetic kpc-scale filaments, which may be produced by SNe collectively in the disk and/or bulge of the galaxy.

- We show strong evidence for ongoing massive SF in the disk of the galaxy at a rate of ~ 0.05 M$_\odot$ yr^{-1}. The presence of the massive stars is required for the heating of the dust and warm ionized gas. The stars, which tend to be formed in groups, may be responsible for some of the energetic extraplanar cool gas features.

- The relative richness of cool gas in the galactic disk is probably related to the isolation of the galaxy in a low density environment. This gas, while being slowly consumed by the SF, may be replenished by the mass loss of evolved star, mostly in the galactic bulge. The gas appears to be undergoing a circulation between the cool and hot phases via the galactic disk/halo interaction. This circulation becomes possible for the galaxy because of both the low temperature of the mass-loaded hot gas and the inefficiency of ram-pressure stripping in the environment.

- A field S0 galaxy may form mainly from the development of a hot gaseous halo, which stops or slows down the supply of cool gas from the IGM. This development may be a natural consequence of the mass growth of a galaxy, according to recent structure formation simulations. But the inclusion of the galactic feedback as well as the environmental effects, as indicated in the present work, may also be important.

REFERENCES

Barr J. M. et al. 2007, A&A, 470, 173

Bekki K., Couch W. J. & Shioya Y. 2002, ApJ, 577, 651

Bell E. F. & De Jong R. S. 2001, ApJ, 550, 212

Binette L., Magris C. G., Stasińska G. & Bruzual A. G. 1994, A&A, 292, 13

Birnboim, Y. & Dekel, A.2003, MNRAS.345..349

Birnboim, Y., Dekel, A. & Neistein, E. 2007, MNRAS, 380, 339

Bohlin R. C., Savage B. D. & Drake J. F. 1978, ApJ, 224, 132

Calzetti, D., et al. 2007, ApJ, 666, 870

Cantiello M., Blakeslee J. P., Raimondo G. 2007, ApJ, 668, 209

Cappellaro E., Evans R. & Turatto M. 1999, A&A, 351, 459

Collins J. A., Rand R. J., Duric N. & Walterbos R. A. M. 2000, ApJ, 536, 645

Cox A. N. 1999, Allen's Astrophysical Quantities (Fourth Edition)

Dale D. A. et al. 2007, ApJ, 655, 863

David L. P. et al. 2006, ApJ, 653, 207

Draine B. T. et al. 2007, ApJ, 663, 866

Faber S. M., Gallagher J. S. 1976, ApJ, 204, 365

Feigelson E. D. et al. 2002, ApJ, 574, 258

Gilfanov M. 2004, MNRAS, 349, 146

Goto T. et al. 2003, PASJ, 55, 757

Grevesse N. & Sauval A. J. 1998, Space Sci. Rev., 85, 161

Han Z., Podsiadlowski Ph., Lynas-Gray A. E. 2007, MNRAS, 380, 1098

Ho L. C., Filippenko A. V., Sargent W. L. W. 1997, ApJS, 112, 315

Howk J. C. & Savage B. D. 1997, AJ, 114, 2463

Howk J. C. & Savage B. D. 1999, AJ, 117, 2077

Hunter D. A., Elmegreen B. G., Martin E. 2006, AJ, 132, 801

Jarrett T. H. et al. 2003, AJ, 125, 525

Kawata D. & Mulchaey J. S. 2008, ApJ, 672, 103

Kennicutt R. C. 1998, ARA&A, 36, 189

Kennicutt R. C. et al. 2003, PASP, 115, 928

Kereš D., Katz N., Weinberg D. H., & Dave R., 2005, MNRAS, 363, 2

Kereš D. & Hernquist L. 2009, ApJL submitted, astro-ph\0905.2186

Lehnert M. D. & Heckman T. M. 1996, ApJ, 462, 651

Li J. T. et al. 2008, MNRAS, 390, 59

Li Z. Y., Wang Q. D. & Hameed S., 2007, MNRAS, 376, 960

Li Z. Y., Wang Q. D. & Wakker B. P. 2009, MNRAS accepted, astro-ph\0902.3847

Lumb D. H., Warwick R. S., Page M. & De Luca A. 2002, A&A, 389, 93

Malhotra S. et al. 2000, ApJ, 543, 634

Malhotra S. et al. 2001, ApJ, 561, 766

Mannucci F. et al. 2005, A&A, 433, 807

Martig M., Bournaud F., Teyssier R. & Dekel A. 2009, ApJ, submitted, astro-ph\arXiv:0905.4669M

Moran S. M. et al. 2006, ApJL, 641, 97

Morganti R. et al. 2006, MNRAS, 371, 157

Mulchaey, J. S., Davis, D. S., Mushotzky, R.F., & Burstein, D. 2003, ApJS, 145, 39

Neistein, E., et al. 1999, ApJ, 117, 2666

Peimbert, M. 1993, in IAU Symp. 155, Planetary Nebulae, ed. R. Weinberger & A. Acker (Dordrecht: Kluwer), 523

Pellegrini S. 1994, A&A, 292, 395

Pellegrini S. 2005, ApJ, 624, 155

Plana H. et al. 1998, A&AS, 128, 75

Raley E. A., Shelton R. L. & Plewa T. 2007, ApJ, 661, 222

Revnivtsev M. et al. 2008, A&A, 490, 37

Rieke G. H. et al. 2009, ApJ, 692, 556

Rossa J. et al. 2008, astro-ph\arXiv:0804.3819

Sage L. J., Welch G. A. 2006, ApJ, 644, 850

Tang S. K., Wang Q. D., Mac Low M. M. & Joung M. R. 2009, astro-ph\arXiv:0902.0386

Temi P., Brighenti F. & Mathews W. G. 2007, ApJ, 660, 1215

Temi P., Brighenti F. & Mathews W. G. 2009, ApJ, 695, 1

Terashima Y., Wilson A. S. 2003, ApJ, 583, 145

Thompson T. W. J., Howk J. C. & Savage B. D. 2004, AJ, 128, 662

Toomre A. 1964, ApJ, 139, 1217

van Dokkum P. G. et al. 1998, ApJ, 500, 714

Wang Q. D. 2004, ApJ, 612, 159

Wang Q. D. 2007, EAS, 24, 59

Welch G. A., Sage L. J. 2003, ApJ, 584, 260

Table 1.   Basic Information of NGC 5866

Parameter	NGC 5866
Morphology[a]	$S0_3$, H II/LINER
Center position[a]	R.A. 15h06m29.5s
(J2000)	Dec. +55d45m47.6s
Distance (Mpc)[a]	11.21 ± 0.80 ($1'' \sim 54$ pc)
Inclination angle[b]	$86.4°$
D_{25} (arcmin)[b]	6.3 ± 0.5
Total B magnitude[b]	10.731 ± 0.074
Total K magnitude[a]	6.873 ± 0.018
Total B-V color[b]	0.85
Foreground Galactic Extinction (E(B-V))[a]	0.013
M_{FIR}[b]	11.044
Galactic foreground $N_H(10^{20}$ cm$^{-2})$[c]	1.46
M_{HI}[d]	$< 1.2 \times 10^8$ M$_\odot$
M_{H_2}[e]	4.39×10^8 M$_\odot$
M_{HII}[f]	4×10^4 M$_\odot$
M_{dust}[g]	4.5×10^6 M$_\odot$
L_{dust}[g]	3×10^9 L$_\odot$
f_{60}/f_{100}[h]	0.29
SFR(M$_\odot$ yr^{-1})[h]	< 0.1
q_{PAH}[g]	2%
M_{dust}/M_H[g]	0.005

Note. — References. - a. NED; b. HYPERLEDA, D_{25} is the diameter at $I_B = 25$ mag arcsec^{-2}, IRAS FIR magnitude $M_{FIR} = -2.5\ log(2.58\ f_{60} + f_{100}) + 14.75$, where f_{60}, and f_{100} are the 60 and 100 μm fluxes, respectively, in Jy; c. HEASARC web tools; d. Sage & Welch 2006; e. Welch & Sage 2003; f. Plana et al. 1998; g. Draine et al. 2007. h. Kennicutt et al. 2003, f_{60}/f_{100} is the IRAS 60 μm to 100 μm flux ratio.

Table 2. *Chandra* Source List

Source	CXOU Name	δ_x ($''$)	CR (cts ks^{-1})	HR	HR1	Flag
(1)	(2)	(3)	(4)	(5)	(6)	(7)
1	J150552.44+554415.8	1.4	1.10 ± 0.32	–	–	B, S
2	J150555.82+554556.9	1.2	1.57 ± 0.39	–	–	B, S
3	J150559.07+554455.2	1.1	1.28 ± 0.35	–	–	B, S
4	J150600.69+554921.6	2.0	0.42 ± 0.18	1.00 ± 0.04	–	H
5	J150601.04+554513.0	0.9	3.46 ± 0.50	-0.03 ± 0.18	0.53 ± 0.20	B, S, H
6	J150603.95+554623.3	0.9	1.28 ± 0.31	–	–	B, S
7	J150605.82+554649.4	0.8	4.70 ± 0.67	–	-0.24 ± 0.15	B, S, H
8	J150608.65+554919.2	1.4	0.40 ± 0.17	1.00 ± 0.02	–	H
9	J150613.31+554359.4	0.7	2.41 ± 0.44	–	–	B, S, H
10	J150616.84+554715.2	0.5	4.29 ± 0.61	-0.26 ± 0.18	-0.06 ± 0.16	B, S, H
11	J150618.38+554547.7	0.7	0.57 ± 0.22	–	–	B
12	J150620.41+554530.3	0.6	0.78 ± 0.22	–	–	B, H, S
13	J150620.46+554622.7	0.4	1.39 ± 0.33	–	–	B, S, H
14	J150620.48+554542.2	0.4	6.69 ± 0.76	-0.27 ± 0.14	0.08 ± 0.14	B, S, H
15	J150620.66+554221.4	1.0	0.46 ± 0.17	–	–	B, H
16	J150620.76+554442.7	0.6	0.37 ± 0.20	-1.00 ± 0.09	–	S
17	J150621.30+554906.7	0.6	5.27 ± 0.74	-0.18 ± 0.17	-0.00 ± 0.17	B, S, H
18	J150621.36+554344.1	1.1	0.44 ± 0.22	–	–	B
19	J150622.50+554721.8	0.6	1.02 ± 0.31	–	–	S, B
20	J150623.05+554542.1	0.7	0.82 ± 0.28	–	–	B, S
21	J150624.53+554707.5	0.8	0.57 ± 0.20	–	–	B, S, H
22	J150625.18+554556.6	0.5	0.77 ± 0.23	–	–	B, S
23	J150627.77+554537.8	0.5	0.89 ± 0.27	–	–	B, S, H
24	J150628.11+554631.6	0.9	0.87 ± 0.27	–	–	B, S
25	J150628.43+554556.4	0.7	0.92 ± 0.29	–	–	B
26	J150628.73+554555.1	0.5	2.10 ± 0.41	–	–	B, H, S
27	J150628.75+554538.7	0.5	1.83 ± 0.37	–	–	B, S, H
28	J150629.14+554551.4	0.8	0.56 ± 0.21	–	–	B
29	J150629.15+554515.6	0.7	0.54 ± 0.20	–	–	B, S
30	J150629.51+554547.5	0.6	0.61 ± 0.20	1.00 ± 0.10	–	H, B
31	J150629.65+554552.7	1.2	0.69 ± 0.25	–	–	B
32	J150629.73+554309.0	0.4	6.30 ± 0.76	-0.59 ± 0.14	-0.02 ± 0.13	S, B, H
33	J150629.84+554533.2	0.6	0.79 ± 0.26	–	–	B, S
34	J150630.33+554648.8	0.6	0.32 ± 0.13	1.00 ± 0.01	–	H, B
35	J150630.43+554139.5	0.6	8.65 ± 1.10	-0.37 ± 0.14	0.03 ± 0.15	B, S, H
36	J150630.45+554515.4	0.7	0.63 ± 0.21	–	–	B, H
37	J150631.26+554458.1	0.5	1.80 ± 0.38	–	–	B, S, H
38	J150631.58+554251.3	0.6	0.92 ± 0.29	–	–	B, S, H
39	J150631.83+554232.3	0.7	0.82 ± 0.25	–	–	B, S, H
40	J150632.17+554220.7	0.6	0.94 ± 0.23	0.86 ± 0.14	–	B, H

Table 2—Continued

Source	CXOU Name	δ_x ($''$)	CR (cts ks^{-1})	HR	HR1	Flag
(1)	(2)	(3)	(4)	(5)	(6)	(7)
41	J150632.70+554658.9	0.5	1.96 ± 0.35	–	0.81 ± 0.18	B, S, H
42	J150632.73+554525.6	0.6	0.46 ± 0.17	–	–	B, H, S
43	J150634.07+554536.6	0.7	0.68 ± 0.23	–	–	B, H, S
44	J150635.60+554445.6	1.7	0.41 ± 0.18	–	–	B
45	J150635.78+554531.4	0.6	0.51 ± 0.21	1.00 ± 0.01	–	B, H
46	J150637.04+554527.3	1.7	0.33 ± 0.18	1.00 ± 0.02	–	B
47	J150638.02+554842.2	0.5	2.88 ± 0.50	–	–	B, S, H
48	J150638.74+554505.6	0.6	1.16 ± 0.32	–	–	B, S, H
49	J150640.17+554612.5	1.4	0.33 ± 0.14	–	–	H, B
50	J150640.26+554514.0	0.9	0.52 ± 0.22	–	–	B, S
51	J150640.48+554806.6	0.4	2.49 ± 0.47	–	–	S, B, H
52	J150643.97+554522.9	0.7	0.46 ± 0.17	–	–	B, H, S
53	J150645.29+554845.3	0.6	0.40 ± 0.19	1.00 ± 0.01	–	B
54	J150652.51+554639.5	1.0	0.45 ± 0.19	–	–	B, H
55	J150653.12+554800.1	0.6	0.70 ± 0.24	–	–	B, H
56	J150653.79+554432.9	0.5	1.32 ± 0.55	–	–	B, S, H
57	J150655.64+554437.7	0.5	0.56 ± 0.19	–	–	B, H
58	J150656.64+554550.5	0.4	1.99 ± 0.38	–	–	B, H, S
59	J150701.15+554715.6	0.9	1.16 ± 0.67	–	–	B, S
60	J150703.66+554833.4	1.7	0.93 ± 0.54	–	–	B
61	J150703.70+554900.6	1.2	0.59 ± 0.23	–	–	B, H
62	J150704.60+554448.9	0.7	2.93 ± 1.06	–	–	S, B
63	J150707.34+554435.4	1.0	0.44 ± 0.18	1.00 ± 0.01	–	H, B
64	J150707.50+554527.1	1.0	1.53 ± 0.73	–	–	B
65	J150708.00+554613.9	0.6	12.63 ± 2.11	-0.30 ± 0.15	-0.42 ± 0.13	B, S, H
66	J150708.48+554545.8	0.7	1.33 ± 0.32	–	–	B, H
67	J150708.78+554144.7	1.3	2.34 ± 0.69	1.00 ± 0.00	–	B, H
68	J150715.72+554955.2	2.1	1.03 ± 0.40	–	–	B, S
69	J150719.26+554449.3	1.0	6.12 ± 1.16	-0.13 ± 0.17	–	B, S, H
70	J150721.08+554559.0	1.0	45.48 ± 3.75	-0.31 ± 0.07	-0.25 ± 0.08	B, S, H
71	J150736.05+554605.6	2.3	1.85 ± 0.81	–	–	B, S

Note. — The definition of the bands: 0.3–0.7 (S1), 0.7–1.5 (S2), 1.5–3 (H1), and 3–7 keV (H2). In addition, S=S1+S2, H=H1+H2, and B=S+H. Column (1): Generic source number. (2): *Chandra* X-ray Observatory (unregistered) source name, following the *Chandra* naming convention and the IAU Recommendation for Nomenclature (e.g., http://cdsweb.u-strasbg.fr/iau-spec.html). (3): Position uncertainty (1σ) calculated from the maximum likelihood centroiding and an approximate off-axis angle (r) dependent systematic error $0\rlap{.}''2 + 1\rlap{.}''4(r/8')^2$ (an approximation to Fig. 4 of Feigelson et al. 2002), which are added in quadrature. (4): On-axis source broad-band count rate — the sum of the exposure-corrected count rates in

the four bands. (5-6): The hardness ratios defined as $HR = (H - S2)/(H + S2)$, and $HR1 = (S2 - S1)/S$, listed only for values with uncertainties less than 0.2. (7): The label "B", "S", or "H" mark the band in which a source is detected with the most accurate position that is adopted in Column (2).

Table 3. Properties of Individual Dust Features

Feature No. (1)	Feature ID (2)	$\lvert z \rvert$ (pc) (3)	a_B (mag) (4)	a_V (mag) (5)	N_H (10^{20} cm^{-2}) (6)	n (cm^{-3}) (7)	M (10^4 M$_\odot$) (8)	Ω (10^{51} ergs) (9)
01	$D - 012 + 002$	110	0.55	0.45	8.0	3.3	5	3
02	$D - 008 + 003$	150	0.41	0.32	5.7	2.3	10	10
03	$D - 004 + 002$	100	0.78	0.56	10.1	6.2	5	2
04	$D + 000 + 003$	140	0.31	0.22	3.9	4.9	2	2
05	$D + 001 + 005$	270	0.10	0.07	1.2	0.9	1	3
06	$D + 002 + 002$	120	0.47	0.37	6.7	8.3	2	1
07	$D + 008 + 004$	190	0.17	0.11	2.0	1.0	2	3
08	$D + 004 - 001$	70	0.39	0.29	5.1	3.2	1	0.3
09	$D + 001 - 001$	80	0.16	0.11	2.0	2.5	0.5	0.2
10	$D - 001 - 001$	70	0.43	0.31	5.5	4.6	1	0.3
11	$D - 003 - 002$	90	0.36	0.22	4.0	3.8	2	0.6
12	$D - 008 - 001$	80	0.36	0.29	5.3	2.8	3	0.8
13	$D - 010 - 001$	70	0.40	0.32	5.7	2.8	4	0.9
14	$D - 013 - 001$	60	0.42	0.31	5.6	7.0	2	0.3
15	$D - 016 - 002$	90	0.41	0.32	5.8	3.6	4	2
16	$D + 008 + 014$	780	0.14	0.11	1.9	1.2	10	17

Note. — (1) Dust feature numbers as marked in Fig. 5. (2) Feature identification in form of $D \pm XXX \pm ZZZ$, where XXX is the distance in arcseconds from the galaxy's optical center along the major axis, while ZZZ is the height in arcseconds from the mid-plane of the galaxy. (3) Physical height of the dust features from the mid-plane. (4) and (5) Apparent extinction in the B and V band. (6) Hydrogen column density. (7) Number density. (8) Gas mass. (9) Gravitational energy.